HHS Public Access

Author manuscript

Neuron. Author manuscript; available in PMC 2018 February 08.

Published in final edited form as:

Neuron. 2017 February 08; 93(3): 509–521.e3. doi:10.1016/j.neuron.2016.12.031.

Flexible near field wireless optoelectronics as subdermal implants for broad applications in optogenetics

Gunchul Shin[1,16], **Adrian M. Gomez**[2,16], **Ream Al-Hasani**[2,16], **Yu Ra Jeong**[3,16], **Jeonghyun Kim**[1,16], **Zhaoqian Xie**[4,16], **Anthony Banks**[1], **Seung Min Lee**[1], **Sang Youn Han**[1,5], **Chul Jong Yoo**[6], **Jong-Lam Lee**[6], **Seung Hee Lee**[6], **Jonas Kurniawan**[1], **Jacob Tureb**[1], **Zhongzhu Guo**[1], **Jangyeol Yoon**[1], **Sung-Il Park**[7], **Sang Yun Bang**[8], **Yoonho Nam**[1], **Marie C. Walicki**[2], **Vijay K. Samineni**[2,9], **Aaron D. Mickle**[2,9], **Kunhyuk Lee**[1], **Seung Yun Heo**[1], **Jordan G. McCall**[2,9], **Taisong Pan**[10], **Liang Wang**[11], **Xue Feng**[12], **Taeil Kim**[13], **Jong Kyu Kim**[6], **Yuhang Li**[14], **Yonggang Huang**[4], **Robert W. Gereau IV**[2,9,15], **Jeong Sook Ha**[3,*], **Michael R. Bruchas**[2,9,15,17,*], and **John A. Rogers**[1,*]

[1]Department of Materials Science and Engineering, Frederick Seitz Materials Research Laboratory University of Illinois at Urbana-Champaign, Urbana, IL 61802, USA

[2]Department of Anesthesiology, Division of Basic Research, Washington University School of Medicine, St. Louis, MO 63110, USA

[3]Department of Chemical and Biological Engineering, Korea University, Seoul, Republic of Korea KU-KIST Graduate School of Converging Science and Technology, Korea University, Seoul 136-701, Republic of Korea

[4]Departments of Civil and Environmental Engineering, Mechanical Engineering, Materials Science and Engineering, Center for Engineering and Health and Skin Disease Research Center Northwestern University, Evanston, IL 60208, USA

[5]Display Research Center, Samsung Display Co. Yongin, Gyeonggi-do 446-920, Republic of Korea

[*]To whom correspondence should be addressed: John A. Rogers, Ph.D; Department of Materials Science and Engineering, Frederick Seitz Materials Research Laboratory University of Illinois at Urbana-Champaign, Urbana, IL, 61801 Tel: 217-244-4979, jrogers@illinois.edu and Michael R. Bruchas, Ph.D; Department of Anesthesiology, Neuroscience, Washington University School of Medicine, 660 South Euclid Ave., Box 8054 St. Louis, MO 63110 Tel: 314-747-5754, bruchasm@wustl.edu and Jeong Sook Ha, Ph.D; Department of Chemical and Biological Engineering, Korea University, Seoul, Republic of Korea KU-KIST Graduate School of Converging Science and Technology, Korea University, Seoul Tel: +82-2-3290-3303, jeongsha@korea.ac.kr.

[16]Co-first author

[17]Lead contact

Author Contributions

Conceptualization, G.S., A.M.G., R.A., J.K., A.B., S.M.L., S.-I.P., J.G.M., R.W.G, M.R.B. and J.A.R; Methodology, G.S., A.M.G., R.A., Y.R.J., J.K., A.B., J.G.M., T.-I.K., M.R.B. and J.A.R; Formal Analysis, J.K., Z.X., S.Y.B., K.L., T.P., L.W., X. F. and Y. L.; Investigation, G.S., Y.R.J., A.M.G., R.A., J.K., Z.X., J.K., J.T., Z.G., S.Y.H., C.J.Y., J.-L.L., S.H.L., J.Y., Y.H.N., M.C.W., V.K.S., A.D.M., S.Y.H., J.K.K.; Writing-Original Draft, G.S., A.M.G., R.A. and Z.X.; Writing-Review & Editing, G.S., A.M.G., R.A., Y.R.J., J.K., Z.X., J.G.M, Y.H., R.W.G., J.S.H., M.R.B. and J.A.R.; Visualization, G.S., A.M.G., R.A., Y.R.J., J.K. and Z.X.; Supervision, J.S.H., R.W.G, M.R.B. and J.A.R.

[6]Department of Materials Science & Engineering, Pohang University of Science & Technology (POSTECH) Pohang, Gyeongbuk 790-784, Republic of Korea

[7]Department of Electrical Engineering, Texas A&M University, College Station, TX 77843, USA

[8]Department of Electrical and Computer Engineering, New York University, Brooklyn, NY 11201, USA

[9]Washington University Pain Center, Washington University School of Medicine, St. Louis, MO 63110, USA

[10]State Key Laboratory of Electronic Thin films and Integrated Devices, University of Electronic Science and Technology of China, Chengdu, Sichuan 610054, P.R. China

[11]Institute of Chemical Machinery and Process Equipment, Zhejiang University, Hangzhou 310027, P.R. China

[12]AML, Department of Engineering Mechanics, Center for Mechanics and Materials, Tsinghua University, Beijing 100084, China

[13]School of Chemical Engineering, Sungkyunkwan University (SKKU), Suwon, Gyeonggi-do 440-746, Republic of Korea

[14]Institute of Solid Mechanics, Beihang University, Beijing 100191, China

[15]Department of Neuroscience, Washington University School of Medicine, Department of Biomedical Engineering, Washington University, St. Louis, MO 63110, USA

Summary

In vivo optogenetics provides unique, powerful capabilities in the dissection of neural circuits implicated in neuropsychiatric disorders. Conventional hardware for such studies, however, physically tethers the experimental animal to an external light source limiting the range of possible experiments. Emerging wireless options offer important capabilities that avoid some of these limitations, but the current size, bulk, weight, and wireless area of coverage is often disadvantageous. Here, we present a simple but powerful setup based on wireless, near-field power transfer and miniaturized, thin flexible optoelectronic implants, for complete optical control in a variety of behavioral paradigms. The devices combine subdermal magnetic coil antennas connected to microscale, injectable LEDs, with the ability to operate at wavelengths ranging from ultraviolet to blue, green/yellow, and red. An external loop antenna allows robust, straightforward application in a multitude of behavioral apparatuses. The result is a readily mass-producible, user-friendly technology with broad potential for optogenetics applications.

Introduction

Understanding and controlling the function of the brain is a challenge in modern neuroscience. Techniques in electrical brain stimulation, based on penetrating or surface mounted electrodes, represent the most traditional means for activating neurons to determine their roles in cognitive function (Campbell et al., 1991; Cogan, 2008; Kozai et al., 2012). Confounding thermal effects, lack of cell-type specificity, the inability to target small numbers of neurons inside electrically conductive tissues and adverse long-term effects on

tissue health are some of the many limitations of these approaches (Aravanis et al., 2007). Optogenetics avoids these complications through the use of photosensitive ion channels or proteins in genetically modified neurons to allow optical stimulation or inhibition of activity in a highly targeted and controlled fashion (Boyden et al., 2005; Deisseroth, 2011; Fenno et al., 2011; Packer et al., 2013; Siuda et al., 2015a, b; Sparta et al., 2012; Toettcher et al., 2011; Yizhar et al., 2011). This methodology is considered as essential for current efforts in neuroscience research largely due to its capabilities for sophisticated functional studies in the central and peripheral nervous systems (Bonin et al., 2015; Boyden et al., 2005; Iyer et al., 2014; Kim et al., 2013; Sparta et al., 2012; Towne et al., 2013). Recent developments in material science and electrical engineering combine this optical control with the use of soft, flexible optoelectronic implants that deliver light directly to regions of interest using ultraminiaturized light emitting diodes (LEDs), powered and controlled wirelessly (Jeong et al., 2015; Kim et al., 2013; McCall et al., 2013; Park et al., 2015a, b). Such devices enable a range of experiments with untethered, freely behaving animals, in isolation or in social groups, and in simple or elaborate environments. Alternative technologies offer similar capabilities, but in more rigid formats (Montgomery et al., 2015). These wireless platforms bypass the constraints associated with traditional optical fiber interfaces and its external connections, however, even the most advanced wireless systems have drawbacks. These include reliance on (1) specialized device architectures and unusual combinations of materials that are not easily adapted to mass manufacturing and (2) wireless operation in radio frequency (RF) bands that are susceptible to signal reflection, interference and absorption by metallic objects, water features, and other obstructions within or adjacent to the area of interest. As a result, such technologies require expertise in RF electronics for optimized configuration and reliable operation. Options in solar and battery power eliminate some of these disadvantages, but they limit experimental options and add significant weight and bulk (Lee et al., 2015; Park et al., 2015b). In all reported approaches, the accessibility of the implantable devices to the broader community is limited due to the specialized procedures required for their construction.

Here, we demonstrate schemes to circumvent these challenges that leverage ideas associated with recently reported, small-scale, flexible optoelectronic devices that achieve wireless operation by inductive coupling at frequencies (13.56 MHz) (Kim et al., 2015a, b) common to those with near field communication (NFC) hardware found in commoditized consumer and industrial wireless electronic devices. In particular, we demonstrate that related NFC schemes and miniaturized, flexible wireless receivers can serve as the basis of a versatile technology for optogenetics. Unlike previous wireless systems designed for the UHF (ultrahigh frequency, 300–3000 MHz) bands, these inductively coupled antennas operate in the HF (high frequency, 3–30 MHz) band. These implantable devices, which use the HF band, overcome the limited operational range associated with previously reported systems (Hannan et al., 2014; Harrison et al., 2009). The result enables full wireless coverage across many cage types and environments, with little sensitivity to the presence of objects or physical obstructions, including those environments made of metals or with significant water content. Reliable operation is, in fact, even possible underwater and/or through metallic cages/plates. This level of robustness in function greatly reduces requirements in RF optimization and tuning. In addition to commoditized NFC transmission and control

hardware, these implantable components can be mass manufactured in planar geometries using established processes adapted from the flexible printed circuit industry. In addition, the near field wireless device/system used here can be modified with add-on NFC chips to correspond with sensors or electrodes for additional biological data. Here, we introduce these features in a device that includes ultrathin injectable needles as supports for microscale inorganic LEDs, or μ-ILEDs (Al-Hasani et al., 2015; Jeong et al., 2015; Kim et al., 2013; McCall et al., 2013; Park et al., 2015a, b; Siuda et al., 2015b; Wu et al., 2015) that implant into targeted regions of the deep brain. An electrically connected sub-system integrates a flexible magnetic loop antenna, rectifier and indicator LED that mounts sub-dermally on top of the animal's skull, to offer chronic stability (many months) in operation without any observable adverse effects on the animal movement, brain tissue, or general social behavior. Detailed studies of these devices and affiliated external hardware, including demonstrations *in vivo* for their use in two models of reward seeking behavior, illustrate key aspects of the technology. The results provide a platform for broad application in studies of freely-moving animal behavior within nearly any experimental context.

Results

Designs and operational features of thin, flexible, millimeter-scale devices for wireless, programmed delivery of light into biological tissues for optogenetic experiments

The device incorporates various functional layers (copper metallization), barrier films (parylene and poly(dimethylsiloxane)) and active components (surface mounted chips and μ-ILEDs) fabricated on a substrate of polyimide (75 μm thickness) in an overall planar geometry to facilitate processing by conventional manufacturing techniques. An open architecture allows out-of-plane motion of an injectable needle during manipulation and implantation. This needle incorporates a μ-ILED (270 μm × 220 μm × 50 μm) at the tip. Previous studies summarize aspects of the size, shape, and biocompatibility of such needles for deep brain implantation (Al-Hasani et al., 2015; Jeong et al., 2015; Kim et al., 2013; McCall et al., 2013; Park et al., 2015b; Siuda et al., 2015b). The electrical interface consists of a pair of metal lines that pass along a serpentine interconnect trace to allow vertical and horizontal freedom of motion relative to a connected circular coil (9.8 mm diameter, copper traces: 8 turns, 60 μm width, 18 μm thickness and 80 μm spacing) with surface mounted chips for power transfer and control via magnetic coupling to a separate RF transmission loop antenna operating at 13.56 MHz (Kim et al., 2015a, b). Here, a capacitor (23 pF) provides impedance matching. A Schottky diode rectifies the received RF signals to yield a current source for the μ-ILEDs.

The system includes two separate LEDs: one with blue emission (470 nm) adjacent to the targeted tissue to serve as the source for optogenetic simulation; the other with red emission (650 nm) lies just under the skin next to the coil to provide an externally visible signal of system activation, at a wavelength that is essentially invisible to rodents (Conway, 2007; Jacobs et al., 1991; Jacobs et al., 2007). We refer collectively to this red LED, the coil and associated components as the body of the device. Additional information about the circuit design and the chip components appears in Figure S1A–D. The entire device is depicted next to a USD dime (17.91 mm diameter) to convey a sense of size (Figure 1B) (insets).

After encapsulation with a uniform bilayer of parylene (5 μm) and poly(dimethylsiloxane) (PDMS; 0.5~300 μm), the maximum thickness is 1.3 mm (at the location of the chips for the rectifier), similar to that of the dime (1.35 mm); the minimum thickness is 0.5 mm at the position of the coil and associated interconnect wiring. The needle has a total thickness of 80 ~ 130 μm and a width of 350 μm (cross sectional area: 0.028 ~ 0.0455 mm^2). These dimensions are comparable to those of conventional optical fiber probes with diameters of 200 μm (cross sectional area: 0.0314 mm^2). These miniaturized dimensions, the lightweight construction (~30 mg) and the mechanical flexibility represent attractive characteristics as a versatile platform for wireless delivery of light not only into targeted regions of the brain but also to other organs and tissues. An enlarged image of the μ-ILED on the tip of the needle (350 μm width) appears in Figure 1C (left). The bottom contact pads of both μ-ILEDs bond to corresponding copper features via a solder paste (SMD290SNL250T5, Chipquik). The colorized SEM image of Figure 1C (right) shows a representative trace of the coil, designed to resonate at 13.56 MHz with a Q factor of ~22 and an inductance of ~1.8 μH. Figure 1D shows the device bent to a radius of curvature R=5 mm (left column) and with the serpentine trace stretched to 300% (right column), obtained by the finite element analysis (FEA) and experiments, where the color in FEA represents the effective strain. The minimum R of the coil can reach ~9 mm, and its maximum stretch can reach ~51%, within limits of elastic reversibility (for 0.3% yield strain of copper). For R=5 mm or the serpentine trace stretched to 300%, the maximum effective strain in copper is ~2.0%, which is much lower than its fracture strain (~5%).

Electrical, optical, mechanical, and thermal properties of the devices

Figure 2 summarizes the essential electrical, optical, mechanical, and thermal properties. The current-voltage response and the optical output power highlight the key operational characteristics, which are all consistent with the requirements for most optogenetic studies. An external loop antenna interface to an RF generator (Feig system; 12 W output power) can wirelessly supply sufficient power for device operation at distances of up to 30 cm. To increase the distance or to operate multiple antennas, the RF signal can be divided with a multiplexer (ID ISC.ANT.MUX, Feig system). The optical output power estimated from the measured current-voltage curve is on the right y-axis of Figure 2A. Most optogenetic experiments require powers of 1~50 mW/mm^2 (Al-Hasani et al., 2015; Aravanis et al., 2007; Boyden et al., 2005, Deisseroth, 2011; Fenno et al., 2011; Jeong et al., 2015; Kim et al., 2013; Montgomery et al., 2015; Park et al., 2015a; Wentz et al., 2011; Yeh et al., 2013; Yizhar et al., 2011), well within the range accessible with these devices, over distances that span the dimensions of most home cage environments and behavioral chambers widely used in small animal behavior experiments. Optical emission in the ultraviolet (UV), blue, green, yellow and red enables activation of the most popular opsins, including Channelrhodopsin-2 (ChR2) halorhodopsin (eNPHR), and archaerhodopsin (Arch or ArchT), SWTCHR, Opto-XRs, and others (Aravanis et al., 2007; Bonin et al., 2015; Boyden et al., 2005; Deisseroth, 2011; Fenno et al., 2011; Iyer et al., 2014; Kim et al., 2013; Packer et al., 2013; Siuda et al., 2015a,b; Sparta et al., 2012; Toettcher et al., 2011; Towne et al., 2013; Yizhar et al., 2011). This entire wavelength range can be addressed in devices that incorporate appropriate μ-ILEDs, as shown in images and emission spectra in Figure 2B. Fabrication of UV devices (390 nm; 100 μm × 100 μm × 6 μm) exploits previously reported lithographic processes

(Kim et al., 2013; McCall et al., 2013). The blue (470 nm; 220 μm × 270 μm × 50 μm) and green (540 nm; 220 μm × 270 μm × 50 μm) devices use commercial μ-ILEDs. The yellow (580 nm; 220 μm × 270 μm × 50 μm) and red (650 nm; 220 μm × 270 μm × 50 μm) devices use yellow and red phosphors (Figure S2A–B) coated onto blue μ-ILEDs, respectively.

The encapsulation bilayer of parylene (5 μm)/PDMS (0.5 ~ 500 μm) extends across all surfaces. Immersion in physiological saline solutions at different temperatures (37, 60 and 90 °C) reveals that these layers provide barrier properties that enable sufficient operational stability. The devices also remain intact, without noticeable degradation of optical power, for at least 90 days at temperatures <90°C (Figure 2C). Based on Arrhenius scaling, the encapsulated devices are projected to survive up to a year at 37 °C in saline solution (Kittel and Kroemer, 1980). Additionally, the optical power is invariant to extension of the serpentine interconnect trace to 300 % (Figure 2D) and bending of the coil to a radius of curvature as small as 6 mm (Figure 2E), which is smaller than that of mouse skull (~7 mm) measured with the caudal view of mouse skull (Bab et al., 2005). Detailed modeling results and mechanical characteristics appear in the Figure S1. This level of flexibility allows the device to be bent over the curved surface of the skull after injecting the needle into the brain. The device is secured and then the skin is sutured over the device.

Thermal considerations are important to the operation of any active device implanted in the brain or other sensitive biological tissues. Infrared imaging reveals no measurable changes in the temperature across the surfaces of the body of the device, including the coil, the red μ-ILED, the rectifier and capacitors, during wireless operation of the blue μ-ILED at light output power up to 50 mW/mm^2 in the air (Figure S2C–D). Careful measurements of temperature at the surface of the blue μ-ILED (Figure 2F; Experimental (E)) as a function of the duty cycle during pulsed operation at three different peak optical powers compare well to those computed using three dimensional thermal models (Figure 2F; Theoretical (T)). Additional modeling results appear in the Figure S2E–H. The data indicate only minute increases in temperature (~0.1 °C) during operation under typical conditions used for most *in vivo* applications, e.g. output power of 10 mW/mm^2 and 20 Hz pulsing at a duty cycle of 20%. Here, the RF transmission system that couples to the loop antenna defines the pulsing parameters. Figure 2G shows representative pulse sequences based on square waveforms at various frequencies (5, 10 and 20 Hz), with light output measured using a low capacitance and high speed photodiode (PDB-C609-2 Silicon Photodiode, API Inc.) placed on top of the operating μ-ILED. The waveforms (controlled via Arduino) have rise and fall times of < 0.1 ms.

In addition to the device coil, the transmission loop antenna must be optimized for efficient power transfer. The voltage induced in the receiving coil depends on the distance from the loop and on their relative angular orientations. A single transmission loop with dimensions of 30 cm × 30 cm shows uniform in-plane coverage (Ratio of output power from the center point > 0.6), although with limited out-of-plane range, such that only 40% of the maximum optical output appears at a vertical distance of 4 cm from the loop. (Figure S3B). A double transmission loop design addresses this limitation. Figure 3A shows a representative configuration, consisting of a double loop antenna with turns at heights of 4 cm and 11 cm from the bottom of the animal enclosure. This figure also shows the optical output power,

normalized by its value at the center of double loop antenna (at 3 cm), for a horizontal device at the height 3 cm, 6 cm, 9 cm and 12 cm. The power is relatively uniform across the region of interest, with the in-plane ratio of the power to its value at the center (at the same height) >0.6, and out-of-plane ratio (normalized by its value at height 6cm) >0.8. Additional experiments for dual loops with spacings of 8, 10 and 13 cm (Figure S3C–E) yield reduced uniformity in coverage compared to the 7 cm spacing in Figure. 3A.

The power also depends on the orientation of the device with respect to the loop antenna. Figure 3B gives the theoretical (T) and experimental (E) results for the power versus the height at three representative positions (center A; edge B; and corner C) and a wide range of angle from 0° to 80°. Here the power is normalized by its value at the center point (A) with height 3 cm and angle 0°. The normalized power values are 0.8~1.5, 0.6~1.4, 0.5~0.9 and 0~0.9 for angles of 0°, 30°, 60° and 80°, respectively. The practical significance of these angular variations must be considered in use of these devices for optogenetics experiments. Advanced antennas and RF delivery schemes offer some potential to minimize these effects.

The spatial uniformity can be visualized directly by simultaneous operation of a large collection of devices (thirteen in this case) placed on a transparent thin substrate inside an enclosure surrounded by a dual loop antenna (30 cm × 30 cm × 15 cm), as in Figure 3C–F. These observations are consistent with those suggested by calculations, and they also illustrate the ability of this system to operate many devices at once, consistent with the expected relationship between the power transfer and the size of the loop antenna (Cannon et al., 2009). Data from such experiments can be captured using a calibrated photodiode to measure the outputs of each μ-ILED. The voltage-output power data, as shown in figure 2A, yields corresponding operating voltages. At heights of 3, 6, 9, and 12 cm from the bottom, devices at the same in-plane positions across the enclosure exhibit maximum variations in the output intensity of only 30%.

Surgical procedure for device implantation

Implantation of these devices (Figure 4A) is very similar to implantation of traditional optic fiber ferrules and previous wireless devices (Al-Hasani et al., 2015; Jeong et al., 2015; Kim et al., 2013; McCall et al., 2013; Siuda et al., 2015b). Once the region of interest has been located and a hole drilled through the skull the device can be lowered using the custom mounting fixture. This fixture holds the needle and the coil, and connects to the arm of a stereotaxic stage from where it can be lowered into the brain (Figure 4B–F). Once the device has been lowered to the required depth the needle is secured in place by applying a small amount of cyanoacrylate gel followed by an accelerant (or approved adhesive, dental cement, etc.). The device can then be released from the fixture by removing the pin (Figure 4G). The coil is then tucked under the skin and can be further secured, although not necessary, with cyanoacrylate gel and the skin sutured (Figure 4H). These surgeries are substantially faster than the implantation of traditional fiber optics and fully sutured without any open skin so the animals recover faster and experiments can begin 4–5 days post-surgery rather than 7–10 days post-surgery. In addition, these devices have a red LED indicator, which is easily visible through the skin, thereby providing a convenient indicator of operation, which has not been previously possible with any reported implantable optogenetic

device (Figure 4I). Figure 4J–L show an implanted animal at various time points after the surgery. Additional images from surgical implantation and data are in Figure S4. *In vivo* measurements yield qualitatively consistent results. More than 80% (19 of 23) of successfully implanted devices survived more than 3 months inside the brain and under the skin.

Adaptation and demonstration of the devices in multiple behavioral apparatuses

Depending on the dimensions of the animal behavior chamber, double loop and/or diagonal loop antennas can increase the volumetric and angular coverage of the near field wireless coverage (Figure 5). Here we show wireless operation and robust coverage in multiple representative cages and boxes commonly used for behavioral studies. Conventional fiber optic approaches or wired hardware cannot be used effectively with enclosed cages (i.e. homecages) or for performing social interaction studies with more than one mouse, due to potential entanglement of the fiber cables, or damage to the head stage. Even wireless systems that rely on UHF cannot operate reliably due to their sensitivity to surrounding metal components and/or water pools/reservoirs in or around the cages (Al-Hasani et al., 2015; Kim et al., 2013; Montgomery et al., 2015; Park et al., 2015a; Siuda et al., 2015b; Wentz et al., 2011; Yeh et al., 2013). By contrast, none of these considerations prevents use of the systems we introduce here. In fact, closed-lid homecages with food and water containers are fully compatible, largely independent of materials and structures, suitable for studies of individuals or groups of mice. The homecage shown here has a length of 30 cm, a width of 20 cm and a height of 20 cm. As in Figure 5A, the loop starts at 4 cm from the bottom of one plane and surrounds the cage twice with 7 cm spacing between these two turns. The right top image of Figure 5B shows that the double loop covers the entire volume, as illustrated by simultaneous operation of 15 devices. Mice with red indicators of operation were able to move with ease freely inside the homecage in the bottom frame of Figure 5B, demonstrating that these devices are highly versatile for use in optogenetics studies.

To demonstrate successful operation in *in vivo* optogenetic experiments, we characterized the technology in a host of commonly sized animal behavior chambers. In two demonstrations, we optogenetically targeted dopamine projection neurons of the dopaminergic system. This is a commonly targeted pathway, and facilitates a combination of behavioral models for testing of dynamic range. Such studies involve a real time place preference (RTPP) box (2 × 30 cm × 30 cm × 30cm) with a modified double coil design as shown in Figure 5C. The coils rest under the box at its center region, to eliminate its influence on natural behaviors of freely moving animals within the box.

As in Figure 5D, the coil covers the dimensions of 30 cm (length), 30 cm (width) and 15 cm (height) which corresponds to a volume of 13.5 liters (13500 cm^3). Mice with working implants appear in the left side of the box in Figure 5D, operated with a modified double loop antenna. See supplemental movie S1 for real time operation in the RTPP box. The Skinner box (Figure 5E), also called an operant conditioning chamber, is widely used for the study and training animals with reward behavior toward various situations and external stimuli. The small but complex structure of the chamber complicates the operation of wired approaches, specifically with regard to the drug addiction field, where an animal is already

tethered to the self-administration line, thus drastically limiting the potential to fully dissect the neural circuitry underlying drug addiction. Additionally, in performing intracranial drug infusions via cannula, one would need two cables, fiber and drug tubing, making these behavioral experiments challenging and difficult to implement. Many metal parts associated with slots on two sides and rod arrays/containers at the bottom can affect the performance and coverage of previously reported wireless systems (Kim et al., 2013; Montgomery et al 2015; Park et al., 2015a; Wentz et al., 2011; Yeh et al., 2013). In this case, mice often stand and lean on the wall for relatively long times due to the small dimensions of the cage and the functioning parts on the wall. The double loop antenna around this small cage yields robust coverage inside the box in a manner that also enhances the angular coverage. Figure 5F shows the placement of double coils and the results of evaluations of coverage using nine devices, as well as a freely moving mouse with an implanted device. See supplemental movie S2–3 for real time operation in the operant chamber. The forced swim test (Figure 5G) is another apparatus of interest for behavioral measures of learned helplessness (Porsolt et al., 1977). Here, the animals can swim and/or entirely submerge in the water, with little effect on the performance. A single loop coil around the water tank covers the area up to 4 cm above and below the surface of the water (Top right: Figure 5H). Figure S5H shows additional experiments in a large water tank and with submerged devices. Additional cage environments, including those with metal running wheels, can be found in Figure S5.

Wireless stimulation of dopaminergic neurons in the VTA or NAc promotes rewarding and reinforcing behaviors

To test for the reliable application of these devices *in vivo*, we targeted the mesolimbic dopaminergic (DA) pathway, a circuit known to facilitate reward and positive reinforcement (Tsai et al., 2009; Witten et al., 2011), by injecting AAV5-DIO-ChR2-eYFP or AAV5-hSyn-FLEX-ChrimsonR-tdTomato into the ventral tegmental area (VTA) of DAT-Cre mice, and directing the injectable μ-ILED unilaterally into the nucleus accumbens (NAc) or ventral tegmental area (VTA). (Figure 6A). Both viral approaches were included to demonstrate the feasibility of stimulating different brain regions, and the functionality of μ-ILED under different emission (blue and red) spectrums. Characterization of robust ChR2 expression in the VTA and NAc is in Figure 6C and D. Here, we demonstrate that within a real-time place preference task wireless photostimulation (20 Hz, 5 ms pulse width) of DAergic terminals in the NAc, as well as DAergic cell bodies in the VTA significantly shifts ChR2- and Chrimson-expressing DAT-Cre mice from no chamber preference to a preference for the stimulation-paired chamber (Figure 6B, E and F; as measured by time in stimulation side – non-stimulation side and % of time in stimulation side). There were no observable differences in chamber preference during no stimulation or stimulation test phases in DAT-Cre mice lacking ChR2 or Chrimson (Figure 6B, E and G). To further demonstrate the feasibility and application of this novel system, we employed an operant self-stimulation paradigm where the mouse is allowed to trigger μ-ILED stimulations on a fixed-ratio 1 schedule of reinforcement where one nosepoke resulted in one photostimulation (Figure 6H). During 7 consecutive days (sessions), both DAT-Cre mice expressing ChR2 and DAT-Cre mice lacking ChR2 were allowed to self-stimulate during 60 min sessions, where a nosepoke in the active port resulted in a μ-ILED stimulation (470 nm, 8 mW, 20 Hz, 5 ms pulse width, 1 sec burst) of dopaminergic terminals within the NAc, while a nosepoke in the

inactive port resulted in no stimulation (Figure 6H). ChR2-expressing DAT-Cre mice significantly preferred the active nosepoke over the inactive nosepoke across 7 sessions, as well significantly received more photostimulations than DAT-Cre mice absent of ChR2 expression (Figure 6I, J and K). When the stimulation was absent, all DAT-Cre mice expressing ChR2 showed a pronounced decrease in active nosepokes (Figure 6L), further indicating that ChR2-expressing mice were exhibiting photostimulation-maintained responding. Taken together, these *in vivo* assays highlight the ability for wireless spatiotemporal targeting of discrete brain regions for broad application in multiple behavioral contexts with regard to *in vivo* optogenetics.

Discussion

The thin, flexible and fully implantable wireless optoelectronic technologies reported here have broad applicability across the neuroscience research community. By comparison to alternatives, the robustness of their operation, the scalable methods for their manufacturing, and the relative simplicity of the associated control and power delivery electronics represent key attractive features. The surgical procedures are similar to those used with conventional optical fiber systems (Boyden et al., 2005; Deisseroth, 2011; Fenno et al., 2011; Sparta et al., 2012; Toettcher et al., 2011; Yizhar et al., 2011) and other wireless systems (Al-Hasani et al., 2015; Jeong et al., 2015; Kim et al., 2013; McCall et al., 2013; Siuda et al., 2015b), but with reduced invasiveness associated with implantation. The lightweight, battery-free, sub-dermal nature of this platform also minimizes collisions between bulky head-mounted hardware and various parts of the cage environment (running wheel, food container, lid and so on) and for avoiding risks that arise from group housing. The sub-dermal configuration allows for long-term functionality as well as simultaneous implantation of the device and the virus during a single surgery rather than two separate surgeries. With traditional fiber optics, the virus is often injected weeks prior to the fiber optic to allow for viral incubation, while also addressing concerns that the external ferrule may loosen and dislodge the fiber optic cable.

An associated consequence of the physical form and the bilayer encapsulation scheme is that the devices have exceptional viability, with robust operation consistently for more than 3 months post implantation without performance degradation or any significant immune responses. The near-field coupling scheme, together with the unique optical, electrical and mechanical characteristics, provide great versatility in all types of optogenetic stimulation and inhibition experiments. Compatibility with a broad range of LEDs (UV, blue, green, yellow and red), and widely controlled optical output powers (0~100 mW/mm2), and pulsing parameters with short rise/fall times (<0.1 ms) support additional options for optogenetic studies using alternate opsins or light-sensitive proteins. Demonstrations in various optogenetic applications with freely moving animals in complex cages, metal surroundings, or also water tanks support these capabilities. Continuous illumination for inhibition may involve challenges in thermal management, perhaps addressable with the addition of copper metallization along the length of the needle to accelerate thermal diffusion away from the μ-ILEDs.

Although the results presented here involve only a single overall device geometry, the designs are easily adaptable for needles with different lengths, matched to targeted regions of the brain, and emerging from different regions of the device relative to the body, potentially to allow bilateral delivery of light in addition to the potential availability to other rodent models (i.e. rats, prairie voles). Advanced versions can be envisioned that involve multiple needle interfaces to a single device body, with single or multiple μ-ILEDs along the length of the shaft. The shapes and the sizes of the antenna coils can also be altered to match the anatomy and the type of animal; larger coils increase the received power, and therefore the operating range beyond the somewhat modest demonstrations reported here. Other alterations will allow application to alternative optogenetic targets, including the spinal cord and sciatic nerve (Montgomery et al., 2015; Park et al., 2015a). Splitter boxes can enable use of a single set of electronics for operation of multiple antennas around multiple cages with different animals, for highly parallel types of experiments or for targeted control of different individual animals within a group. Advanced antenna designs and transmission electronics have the potential to eliminate current limitations associated with angular variations in the received power, and to expand the operating range to even larger sizes. Furthermore, the same NFC approach for delivering power to the devices can serve, with advanced electronics, as a wireless capability for data communication. For example, with the rapid emergence of sophisticated NFC chips, possibilities such independent control of multiple μ-ILEDs on a single needle, and integration of photodetectors. Previously reported, battery-based technologies in wireless drug delivery (Jeong et al, 2015) could also be considered in wireless embodiments. Such types of customized wireless systems (Figure S6A–D) in the context of mass producible device architectures (Figure S6E–H) foreshadow widespread use for many purposes in neuroscience research.

STAR METHODS

CONTACT FOR REAGENT AND RESOURCE SHARING

Further information regarding reagents and resources may be directed to, and can be fulfilled by the lead contact Michael Bruchas, bruchasm@wustl.edu and devices can now be obtained at www.neurolux.org.

EXPERIMENTAL MODEL AND SUBJECT DETAILS

Adult (25–35 g, ~8–16 weeks of age during experiments) male DAT-Cre mice (species *Mus musculus*) were group housed (no more than 5 littermate per cage) and allowed food and water ad libitum. Mice were maintained on a 12 hr:12 hr light:dark cycle (lights on at 7:00 am). All procedures were approved by the Animal Care and Use Committee of Washington University and adhered to NIH guidelines. DAT-IRES-Cre mice were kindly provided by the laboratory of Xiaoxi Zhuang. The mice were bred at Washington University in St. Louis by crossing the DAT-IRES-Cre mice with C57BL/6 wild-type mice and backcrossed for seven generations.

METHOD DETAILS

Fabrication of implants—The implantable device fabricating process begins with a flexible sheet of electro-deposited (Cu/Polyimide/Cu) high-density material (Dupont,

Pyralux) that is commercially available. The polyimide layer has 75 μm thickness, selected to provide sufficient robustness for injection and but with adequate flexibility to minimize mechanically induced irritation at the tissue interface. Such substrates are compatible with state-of-the-art manufacturing capabilities. When manufactured in panel mode, each sheet (30 cm by 23 cm) can support hundreds of devices. The device pattern was defined on both sides of this flexible substrate using a photolithographic technique followed by an etch process for pattern delineation of the antenna (60 μm traces, 80 μm spaces), injectable needle (75 μm thick, 350 μm wide) and other remaining patterns, all within the range of capabilities of conventional photolithographic tools. The holes (50 μm in diameter) were laser-drilled through the substrate and were subsequently filled with copper by electroplating to form electrical interconnect to both layers. A polyimide cover layer (~25 μm) coated over the entire surface and openings are lithographically defined for the electronic components; μ-ILED (TR2227, Cree Inc.), capacitor (250R05L220GC4T, Johanson Tech), rectifier (CBDQR0130L-HF, Comchip Tech) and indicator (LNJ947W8CRA, Panasonic Elec.) which will then then placed and attached using state-of-the-art tools for component pick-and-place. A UV laser cut all radius and contours including the extendable serpentine electrical interconnect and needle, leaving the device fully suspended by two support chads for ease of handling. After placing and integrating all components including μ-ILED, PDMS and parylene were coated by a simple dip coating processes and commercial deposition equipment. Red (HTR650, Phosphor Tech) and yellow (HTY560, Phosphor Tech) phosphors were used to shift the wavelength of emission from the blue LEDs. Each phosphor powder was mixed with epoxy (5 min curable) at a mass ratio of 5:1. A small amount of this mixture was applied to the entire surface of the LED, and then cured in air for 10 minutes. Figure S2A shows schematic illustrations and pictures of phosphor-coated LEDs. The red phosphor yields red light (peak wavelength= 650 nm) as a result of stimulation from the 470 nm emission from the blue LEDs. Figure S2B shows the shift from blue to red in the emission spectra.

Mechanical modeling—Finite Element Analysis (FEA) using ABAQUS commercial software (ABAQUS Analysis User's Manual 2010, V6.10) allowed calculations of the strains in the device subject to bending and stretching. The thickness of each layer in the cross section of the coil, needle and serpentine trace is given in Figure S1F with their elastic properties in S1E. The other components in the device (capacitor, μ-LEDs, rectifier and red-indicator) are modeled as rigid. As in experiments (Figure 1D), the load in the FEA is applied to bend the device to a radius of curvature as small as 5 mm and stretch the serpentine trace by 300%. The outside layers (Parylene, PDMS and Cu in Figure S1F) are modeled by the composite shell element (S4R), while the thick polyimide layer in the middle is modeled by the 3D, solid hexahedron element (C3D8R). Three mesh densities, with 96,000, 360,000 and 1,360,000 elements, are used to ensure the accuracy and convergence of numerical results, with the relative difference in the maximum strain ~1.5% (Figure S1G–J). The minimal mesh size for 360,000 elements is ~0.1 of the smallest feature dimension.

The effect of device deformation on the output power—The output power of the device depends on the magnetic flux through the device, the resonant frequency and the Q

factor of the device. In general, the magnetic flux $\Phi = \int\int_S B \cdot dS$ through the device decreases with the bending radius due to a decrease in the projected area, where B is magnetic field produced by double loop antenna and S is the in-plane area enclosed by the coil of the device. For a large double loop antenna, the magnetic field B remains essentially the same when a small device is bent such that the magnetic flux Φ depends only on the in-plane area S. The change of S is given by (d/R)2/32, where d is the inner diameter of the device and R is the bending radius of curvature. For the device with ~9.8 mm outer diameter, d=~7.9 mm, the in-plane area S only decreases by ~5.3% for R=6 mm. The magnetic flux therefore almost remains unchanged for R>6mm. The in-plane area S does not change when the serpentine trace is stretched, as shown in Figure 2D. The resonant frequency and Q factor depend on effective inductance L of the coil. Figure S1G shows that the maximum difference between the effective inductance for a planar coil and one with a radius of curvature 6 mm is only ~4.2%. Consequently the output power of the device remains unchanged for a bending radius R>~6 mm, though this conclusion does not hold for R significantly smaller than 6 mm, as shown in Figure 2E. The deformed device obtained from FEA is imported into commercial software (Ansys HFSS 13 User's guide, Ansys Inc. 2011) to study the electromagnetic properties (e.g., Q factor, resonant frequency).

Thermal Characteristics—Temperature changes of the device and μ-ILEDs were monitored with an infrared (IR) camera (A655sc, FLIR systems) and an integrated temperature sensor. Figure S2C–D shows the surface temperature of entire device, including the coil, rectifier, capacitor, red indicator LED and the injectable μ-ILED in air. These measurements revealed no significant changes of the temperature over the entire device. The temperature of the μ-ILED increased by ~1.5 °C for an operating condition of 50 mW/mm^2, 20 Hz, 20% duty cycle after 10 minutes of operation. Modeling results for the temperature of tissue adjacent to an operating device as a function of the output power density and duty cycle appear in Figure S2E–H. The results are similar to experimental findings in Figure 2F. For conditions typical of those used for optogenetic stimulation (< 40% duty cycle, < 50 mW/mm^2), the tissue temperatures increased by less than 0.8 OC. Additional results correspond to measurements using Pt temperature sensors integrated directly next to the μ-ILED during operation inside a warm hydrogel (37 °C).

Light output power measurements—The output power levels of wired μ-ILED devices (Figure 2A) were measured with an optical fiber, an integrating sphere (FOIS-1, Ocean Optics) and a spectrometer (HR 4000, Ocean Optics). The output power levels of wirelessly operating μ-ILEDs were measured with a photodiode (PDB-C609-2 Silicon Photodiode, API Inc.). The measured photocurrent is directly proportional to the optical output power from the μ-ILED at various wireless conditions (position, distance, angle and power). Calibration of the response of the photodiode to μ-ILEDs during wired operation using a separate DC power supply provides the same photocurrent on the photodiode. The voltage-output power data yields the output power density of LED during wireless operation.

Stereotaxic surgery—Mice were anesthetized in an induction chamber (4% isoflurane), placed in a stereotaxic frame (Kopf Instruments), and maintained at 1% – 2% isoflurane. Mice were then injected unilaterally using a blunt needle (86200, Hamilton Com.) with 350

nl of AAV5-DIO-ChR2-eYFP (Hope Center Viral Vector Core, viral titer 2×10^{13} vg/ml) or AAV5-hSyn-FLEX-ChrimsonR-tdTomato (UNC Vector Core) into the VTA (AP −3.2, ML ±0.5, DV −4.8). After allowing 5–6 weeks for sufficient ChR2 to reach the terminal field, mice were then implanted with wirelessly-powered μ-ILED wireless devices with the needle portion of the device containing the μ-ILED implanted into the NAc (AP +1.2, ML ±0.3, DV −4.5 for ChR2-eYFP) or VTA (AP −3.2, ML ± 0.5, DV −4.8 for ChrimsonR-tdTomato). Mice were allowed 7 days of recovery before the start of behavioral experiments.

Real-Time Place Testing (RTPP)—Mice were placed in a custom-made unbiased, balanced two-compartment conditioning apparatus (52.5 × 25.5 × 25.5 cm) as described previously by (Siuda et al., 2015b; McCall et al., 2015; Al-Hasani et al., 2015). Mice underwent a 20 min trial where entry into one compartment triggered a wirelessly-powered photostimulation of 20 Hz (5 ms pulse width) frequency while the mice remained in the stimulation-paired chamber, and entry into the other chamber resulted in no photostimulation (Refer to Figure 5C, D for modeling of wirelessly-powered RTPP setup).

Operant Self-Stimulation—As previously described by (Al-Hasani et al., 2015), mice are initially food deprived to 90% of their body weight and trained to nose poke for food pellets for 4 days during daily 60 min sessions in a mouse modular test chamber (Med Associates Inc.) on a fixed-ratio 1 (FR1) schedule of reinforcement. A correct nose poke response within the active hole resulted in a food pellet delivery where an incorrect nose poke within the inactive hole resulted in no food pellet. This was followed by a 60 min operant self-stimulation session (for 7 consecutive days) where an active nose poke resulted in a 1 sec, 473 nm photostimulation (20 Hz, 5 ms pulse width) where an inactive nose poke resulted in no photostimulation. All active nose pokes were accompanied by a 1 sec illumination of a cue light. (Refer to Figure 5E, F for modeling of wirelessly-powered operant box setup).

Immunohistochemistry—Immunohistochemistry was performed as previously described by (Al-Hasani et al., 2013; Kim et al., 2013; McCall et al., 2015). In brief, mice were intracardially perfused with 4% PFC and then brains were sectioned (30 microns) and placed in 1X PB until immunostaining. Free-floating sections were washed in 1X PBS for 3 × 10 min intervals. Sections were then placed in blocking buffer (0.5% Triton X-100 and 5% natural goat serum in 1X PBS) for 1 hr at room temperature. After blocking buffer, sections were placed in primary antibody (anti-chicken tyrosine hydroxylase (1:1000), Aves Labs, Inc.) overnight at room temperature. After 3 × 10 min 1X PBS washes, sections were incubated in secondary antibody (Alexa Fluor 594 goat anti-chicken (1:1000), Life Technologies) for 2 hrs at room temperature, followed by subsequent washes (3 X 10 min in 1X PBS). Subsequently, sections were incubated in NeuroTrace (435/455 blue fluorescent Nissl stain (1:400), Life Technologies) for 1 hr, followed by 3 × 10 min 1XPBS and 3 × 10 min 1XPB washes. After immunostaining, sections were mounted and coverslipped with Vectashield Hard set mounting medium (Vector Laboratories) and imaged on a Leica TCS SPE confocal microscope.

QUANTIFICATION AND STATISTICAL ANALYSIS

For real-time place preference testing (Fig 6E–G), data are presented as mean ± SEM, and were analyzed by 3-way analyses of variance (ANOVA) with Bonferroni post-hoc tests. RTPP experimental groups are as follows (Blue LED stimulation: n=12/DAT-Cre+, n=5/DAT-Cre−; Red LED stimulation: n=11/DAT-Cre+, n=8/DAT-Cre−). Daily self-stimulation sessions (Fig 6I–K) were analyzed using repeated measures ANOVAs with Tukeys post-hoc tests. Student's t-test was used to determine the significance of active nosepokes between Day 7 stimulation and Day 8 no stimulation test days (Fig. 6L). Self-stimulation experimental groups are as follows: n=6 for DAT-Cre+ and n=5 for DAT-Cre−. All statistically significant analyses were set at $p < 0.05$.

ADDITIONAL RESOURCES

For additional information about commercial versions of this technology now available, please visit www.neurolux.org where devices and hardware can be obtained.

REAGENT or RESOURCE	SOURCE	IDENTIFIER
Antibodies		
Tyrosine Hydroxylase (TH)	Aves Labs	Cat# TYH, RRID:AB_10013440
Goat anti-Chicken, Alexa Fluor 594	Thermo Fisher	Cat# A-11042; AB_2534099
NeuroTrace 435/455	Thermo Fisher	Cat# N21479
Experimental Models: Organisms/Strains		
DAT-Cre mice (B6.SJL-*Slc6a3*$^{tm1.1(cre)Bkmn}$/J)	Cristina M Backman, National Institute on Drug Abuse (NIH)	https://www.jax.org/strain/006660
Viruses		
AAV5-DIO-ChR2-eYFP (1.5 × 10^13 vg/ml)	Washington University HOPE Center Viral Vector Core	https://hopecenter.wustl.edu/?page_id=99
AAV5-hSyn-FLEX-ChrimsonR-tdTomato (5.7×10^12 vg/ml)	University of North Carolina Vector Core	https://www.med.unc.edu/genetherapy/vectorcore

Supplementary Material

Refer to Web version on PubMed Central for supplementary material.

Acknowledgments

This work was supported by an NIH Director's Transformative Research Award (NS081707) to J.A.R, R.W.G, and M.R.B. This work was also supported by EUREKA Fund (DA037152), DA033396 (supplement to A.M.G.) and K99/R00 Pathway to Independence Award to R.A. (DA038725). Y.R.J. and J.S.H. were supported by the National Research Foundation of Korea (NRF) grant funded by the Korean government (MEST) (Grant No. NRF-2016R1A2A1A05004935) and J.S.H. also thanks the KU-KIST graduate school program of Korea University. Z.X. and X.F. acknowledge the support from the National Basic Research Program of China (Grant No.

2015CB351900) and National Natural Science Foundation of China (Grant Nos.11402134, 11320101001). Y.H. acknowledges the support from NSF (DMR-1121262, CMMI-1300846 and CMMI-1400169) and the NIH (grant no. R01EB019337). ADM was supported by the McDonnell Center for Cellular and Molecular Neurobiology Postdoctoral Fellowship and VKS was supported by the Indian American Urological Association/Kailash Kedia, MD Research Scholar Fund.

References

Al-Hasani R, McCall JG, Shin G, Gomez AM, Schmitz GP, Bernardi JM, Pyo CO, Park SI, Marcinkiewcz CM, Crowley NA, et al. Distinct Subpopulations of Nucleus Accumbens Dynorphin Neurons Drive Aversion and Reward. Neuron. 2015; 87:1063–1077. [PubMed: 26335648]

Aravanis AM, Wang L-P, Zhang F, Meltzer LA, Mogri MZ, Schneider MB, Deisseroth K. An optical neural interface: in vivo control of rodent motor cortex with integreated fiberoptic and optogenetic technology. J Neural Eng. 2007; 4:S143–S156. [PubMed: 17873414]

Bab, IA., Hajbi-Yonissi, C., Gabet, Y., Muller, R. Micro-tomographic atlas of the mouse skeleton. Springer Science & Business Media press; 2007.

Bonin RP, Wang F, Desrochers-Couture M, Gasecka A, Boulanger ME, Cote DC, Konick YD. Epidural optogenetics for controlled analgesia. Mol Pain. 2015; 12:1–11.

Boyden ES, Zhang F, Bamberg E, Nagel G, Deisseroth K. Millisecond-timescale, genetically targeted optical control of neural activity. Nat Neurosci. 2005; 8:1263–1268. [PubMed: 16116447]

Cannon BL, Hoburg JF, Stancil DD, Goldstein SC. Magentic resonant coupling as a potential means for wireless power transfer to multiple small receivers. IEEE Trans Power Electron. 2009; 24:1819–1825.

Campbell PK, Jones KE, Huber RJ, Horch KW, Normann RA. A silicon-based, three-dimensional neural interface: manufacturing processes for an intracortical electrode array. IEEE Trans Biomed Eng. 1991; 38:758–768. [PubMed: 1937509]

Cogan SF. Neural stimulation and recording electrodes. Annu Rev Biomed Eng. 2008; 10:275–309. [PubMed: 18429704]

Conway BR. Color vision: Mice see hue too. Curr Biol. 2007; 17:R457–R460. [PubMed: 17580074]

Deisseroth K. Optogenetics. Nat Methods. 2011; 8:26–29. [PubMed: 21191368]

Fenno L, Yizhar O, Deisseroth K. The development and application of optogenetics. Annu Rev Neurosci. 2011; 34:389–412. [PubMed: 21692661]

Hannan HA, Mutashar S, Samad SA, Hussain A. Energy harvesting for the implantable biomedical devices: issues and challenges. Biomed Eng Online. 2014; 13:79. [PubMed: 24950601]

Harrison RR, Kier RJ, Chestek CA, Gilja V, Nuyujukian P, Ryu S, Greger B, Solzbacher F, Shenoy KV. Wireless neural recording with single low-power integrated circuit. IEEE Trans Neural Syst Rehabil Eng. 2009; 17:322–329. [PubMed: 19497825]

Iyer SM, Montgomery KL, Towne C, Lee SY, Ramakrishnan C, Deisseroth K, Delp SL. Virally mediated optogenetic excitation and inhibition of pain in freely moving nontransgenic mice. Nat Biotechnol. 2014; 32:274–278. [PubMed: 24531797]

Jacobs GH, Neitz J, Deegan JF. Retinal recptors in rodents maximally sensitive to ultraviolet light. Nature. 1991; 353:655–656. [PubMed: 1922382]

Jacobs GH, Williams GA, Cahill H, Nathans J. Emergence of novel color vision in mice engineered to express a human cone photopigment. Science. 2007; 315:1723–1725. [PubMed: 17379811]

Jeong J-W, McCall JG, Shin G, Zhang Y, Al-Hasani R, Kim M, Li S, Sim JY, Jang K-I, Shi Y, et al. Wireless Optofluidic Systems for Programmable In Vivo Pharmacology and Optogenetics. Cell. 2015; 162:1–13.

Kim J, Banks A, Cheng H, Xie Z, Xu S, Jang KI, Lee JW, Liu Z, Gutruf P, Huang X, et al. Epidermal Electronics with Advanced Capabilities in Near-Field Communication. Small. 2015a; 11:906–912. [PubMed: 25367846]

Kim J, Banks A, Xie Z, Heo SY, Gutruf P, Lee JW, Xu S, Jang K-I, Liu F, Brown G, et al. Miniaturized Flexible Electronic Systems with Wireless Power and Near-Field Communication Capabilities. Adv Funct Mater. 2015b; 25:4761–4767.

Kim T, McCall JG, Jung YH, Huang X, Siuda ER, Li Y, Song J, Song YM, Pao HA, Kim RH, et al. Injectable, cellular-scale optoelectronics with applications for wireless optogenetics. Science. 2013; 340:211–216. [PubMed: 23580530]

Kittel, C., Kroemer, H. Thermal Physics. 2. Macmillan press; 1980.

Kozai TD, Langhals NB, Patel PR, Deng X, Zhang H, Smith KL, Lahann J, Kotov NA, Kipke DR. Ultrasmall implantable composite microelectrodes with bioactive surfaces for chronic neural interfaces. Nat Mater. 2012; 11:1065. Smit. [PubMed: 23142839]

Lee ST, Williams PA, Braine CE, Lin D-T, John SWM, Irazoqui PP. A miniature, fiber-coupled, wireless, deep-brain optogenetic stimulator. IEEE Trans Neural Syst Rehabil Eng. 2015; 23:655–664. [PubMed: 25608307]

McCall JG, Kim TI, Shin G, Huang X, Jung YH, Al-Hasani R, Omenetto FG, Bruchas MR, Rogers JA. Fabrication and application of flexible, multimodal light emitting devices for wireless optogenetics. Nat Protoc. 2013; 8:2413–2428. [PubMed: 24202555]

Montgomery KL, Yeh AJ, Ho HS, Tsao V, Mohan Iyer S, Grosenick L, Ferenczi EA, Tanabe Y, Deisseroth K, Delp SL, Poon AS. Wirelessly powered, fully internal optogenetics for brain, spinal and peripheral circuits in mice. Nat Methods. 2015; 12:969–974. [PubMed: 26280330]

Packer AM, Roska B, Hausser M. Targeting neurons and photons for optogenetics. Nat Neurosci. 2013; 16:805–815. [PubMed: 23799473]

Park S-I, Brenner DS, Shin G, Morgan CD, Copits BA, Chung hU, Pullen MY, Davidson S, Oh SJ, Yoon J, et al. Soft, stretchable, fully implantable miniaturized optoelectronic systems for wireless optogenetics. Nat Biotechnol. 2015a; 33:1280–1286. [PubMed: 26551059]

Park SI, Shin G, Banks A, McCall JG, Siuda ER, Schmidt MJ, Chung HU, Noh KN, Mun G–H, Rhodes J, et al. Ultraminiaturized photovoltaic and radio frequency powered optoelectronic systems for wireless optogenetics. J Neural Eng. 2015b; 12:056002. [PubMed: 26193450]

Porsolt RD, Bertin A, Jalfre M. Behavioral despair in mice: a primary screening testing for antidepressants. Arch Int Pharmacodyn Ther. 1977; 229:327–336. [PubMed: 596982]

Siuda ER, Copits B, Schmidt MJ, Baird M, Al-Hasani R, Planer WJ, Funderburk S, McCall JG, Gereau RW IV, Bruchas MR. Spatiotemporal control of opioid signaling and behavior. Neuron. 2015a; 86:923–935. [PubMed: 25937173]

Siuda ER, McCall JG, Al-Hasani R, Shin G, Park SI, Schmidt MJ, Anderson SL, Planer WJ, Rogers JA, Bruchas MR. Optodynamic Simulation of b-Adrenergic Receptor Signaling. Nat Commun. 2015b; 6:8480. [PubMed: 26412387]

Sparta DR, Stamatakis AM, Phillips JL, Hovelso N, van Zessen R, Stuber GD. Construction of implantable optical fibers for long-term optogenetic manipulation of neural circuits. Nat Protoc. 2012; 7:12–23.

Tsai H–C, Zhang F, Adamantidis A, Stuber GD, Bonci A, Lecea L, Deisseroth K. Phasic firing in dopaminergic neurons is sufficient for behavioral conditioning. Science. 2009; 324:1080–1084. [PubMed: 19389999]

Toettcher JE, Voigt CA, Weiner OD, Lim WA. The promise of optogenetics in cell biology: interrogating molecular circuits in space and time. Nat Methods. 2011; 8:35–38. [PubMed: 21191370]

Towne C, Montgomery KL, Iyer SM, Deisseroth K, Delp SL. Optogenetic control of targeted peripheral axons in freely moving animals. PLoS One. 2013; 8:e72691. [PubMed: 23991144]

Wentz CT, Bernstein JG, Monahan P, Guerra A, Rodriguez A, Boyden ES. A wirelessly powered and controlled device for optical neural control of freely-behaving animals. J Neural Eng. 2011; 8:046021. [PubMed: 21701058]

Witten IB, Steinberg EE, Lee SY, Davidson TJ, Zalocusky KA, Brodsky M, Yizhar O, Cho SL, Gong S, Ramakrishnan C, et al. Recombinase-driver rat lines: Tools, techniques, and optogenetic application to dopamine-mediated reinforcement. Neuron. 2011; 72:721–733. [PubMed: 22153370]

Wu F, Stark E, Ku PC, Wise KD, Buzsaki G, Yoon E. Monolithically integrated μLEDs on silicon neural probes for high-resolution optogenetic studies in behaving animals. Neuron. 2015; 88:1136–1148. [PubMed: 26627311]

Yizhar O, Fenno LE, Davidson TJ, Mogri M, Deisseroth K. Optogenetics in neural systems. Neuron. 2011; 71:9–34. [PubMed: 21745635]

Yeh AJ, Ho JS, Tanabe Y, Neofytou E, Beygui RE, Poon AS. Wirelessly powering miniature implants for optogenetic stimulation. Appl Phys Lett. 2013; 103:163701.

Highlights

- Subdermal, wireless optogenetic platform for untethered neuronal control
- Thin, flexible devices for discrete spatio-temporal targeting of neural circuits
- Low cost, reliable NFC technology adaptable to most common behavioral contexts
- NFC devices can be tailored for use with different wavelength opsins *in vivo*

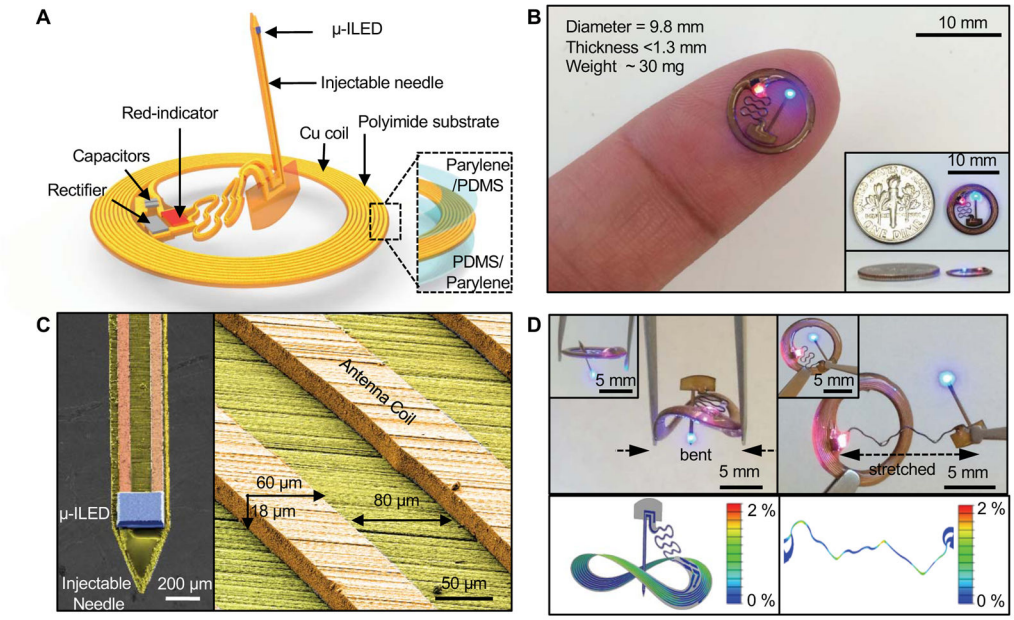

Figure 1. Designs and operational features of a thin, flexible wireless optoelectronic implants for optogenetic experiments

A) Schematic illustration of the overall construction, highlighting a freely adjustable needle with an μ-ILED at the tip end, connected to a receiver coil with matching capacitors, a rectifier and a separate μ-ILED indicator. B) Picture of a completed device (diameter ~9.8 mm) on top of fingertip and next to a US dime (diameter 17.91 mm) (insets) for size comparison. C) Scanning electron microscope images of an injectable needle with LED and coil trace with the dimension of 60 μm width, 18 μm thickness and 80 μm spacing, colorized to highlight the different components (blue: μ-ILED; yellow: polyimide; orange: copper). D) Images and corresponding finite element modeling results of the device before and after bending (left) the body of the device and stretching (right) the serpentine connection to the injectable needle, respectively.

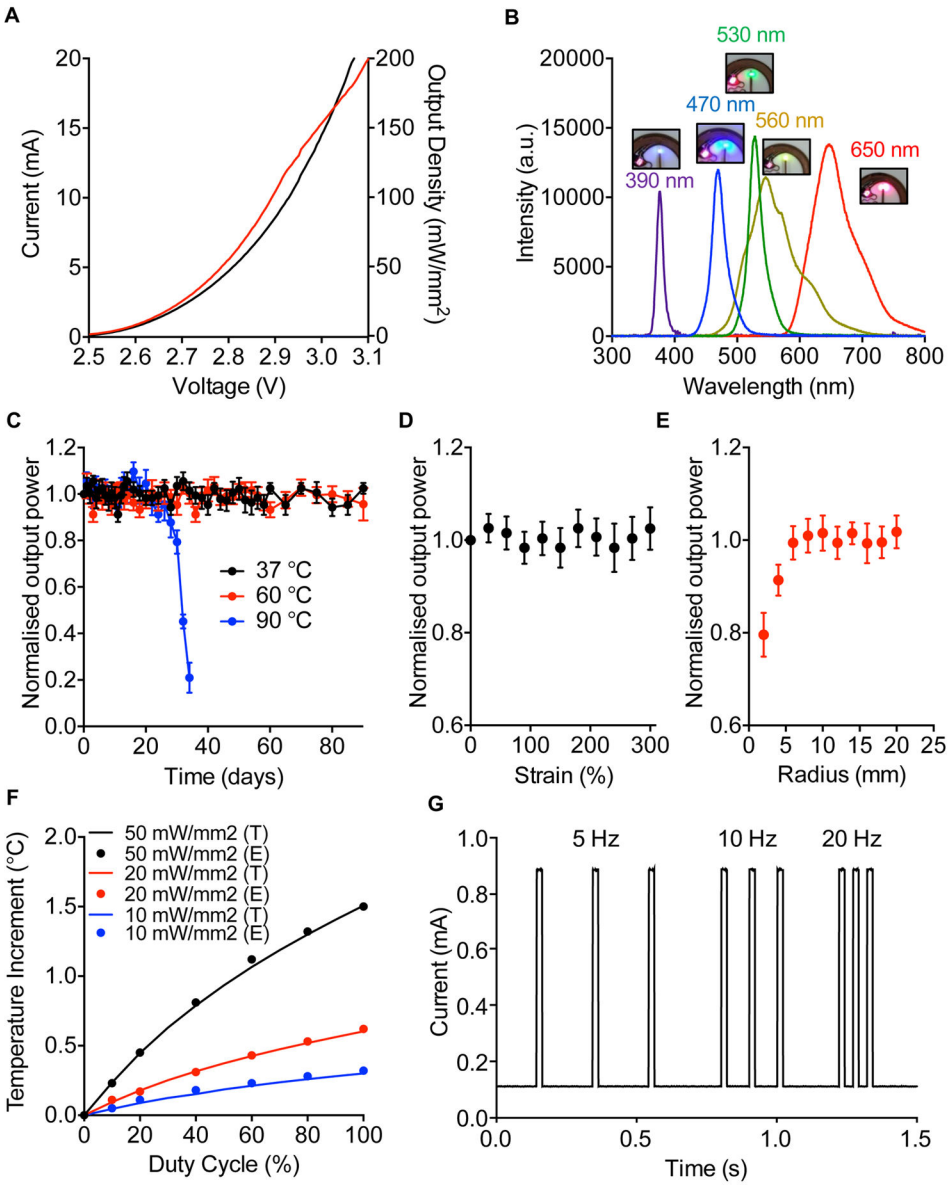

Figure 2. Electrical, optical, mechanical, and thermal properties

A) Current-Voltage-Light output characteristics. B) Emission spectra associated with operation of devices built with different μ-ILEDs. C) Normalized light optical power as a function time after immersion of devices in warm saline solutions with temperatures of 37, 60 and 90 °C. D, E) Normalized light optical as a function of extension of the serpentine interconnect to the injectable needle and of the bending radius of the body of the device, respectively. F) Change in temperature adjacent to an operating μ-ILED (T: Theoretical, for the case of brain tissue; E: Experimental, for the case of a hydrogel) as a function of duty cycle of operation at different peak output powers (10, 20 and 50 mW/mm^2). G) Current output from a photodiode placed adjacent to a μ-ILED operating at different pulse frequencies (5, 10 and 20 Hz), for a fixed duration of 20 ms. The rise and fall times are ~0.1 ms.

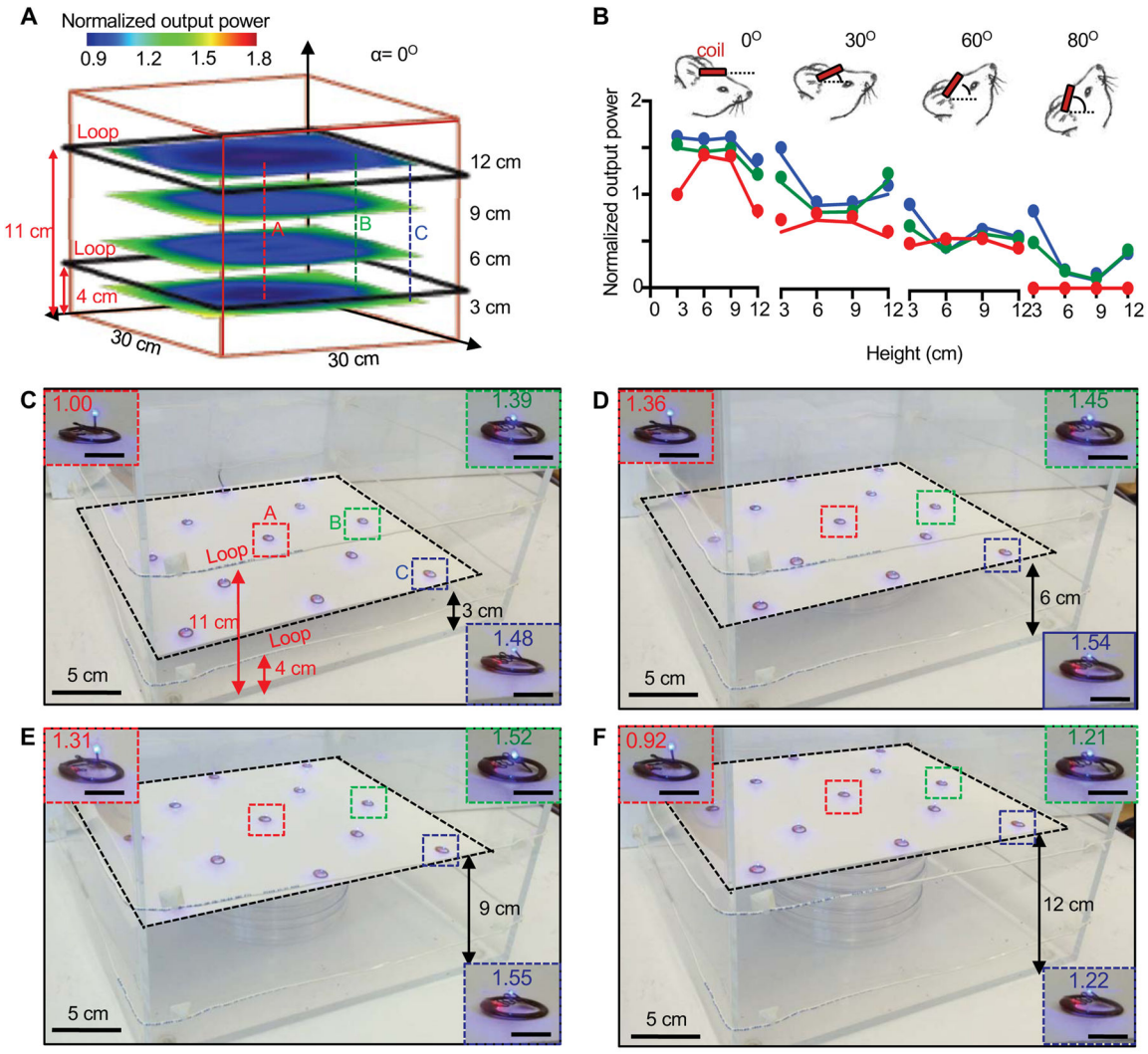

Figure 3. Modeling and experimental results for power transmission from loop antennas with different designs

A) Simulated light output power from a wireless device, as a function of in-plane position at four different heights from the bottom of an enclosure, for the case of a double loop antenna with turns at heights of 4 and 11 cm. B) Theoretical (lines) and experimental (symbols) results for the normalized light output power as a function of height for four different angular orientations between the coil and the loop antennas. The inset cartoons show tilted views of head of the animal. C, D, E, F) Wireless operation of thirteen devices mounted on a thin transparent support, placed at heights of 3, 6, 7 and 12 cm from the bottom. The insets show enlarged images of devices with position of A (red dotted square), B (green dotted square), C (blue dotted square) and normalized light output power.

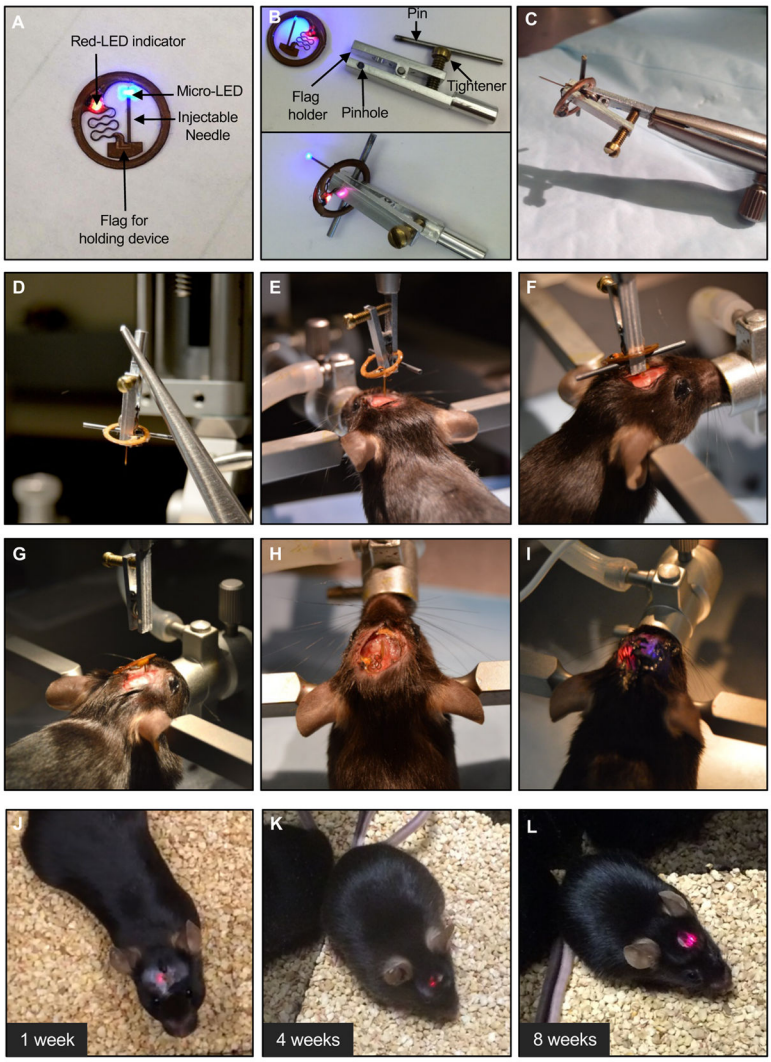

Figure 4. Illustration of surgical procedures for implanting the device and recovered mouse for operation in the deep brain

A) Representative image of implantable device. B) Images of customized mounting clip and its procedure. C) Image after connecting with stereotaxic arm. D, E, F) Images of the surgical steps for holding and positioning the body of the device, and injecting the needle into the deep brain, respectively. G, H) Images of mouse after releasing of device from stereotaxic arm. I) Wireless operation of implanted device after suturing the skin. J, K, L) Images of recovered mouse after 1, 4 and 8 weeks from surgery, respectively.

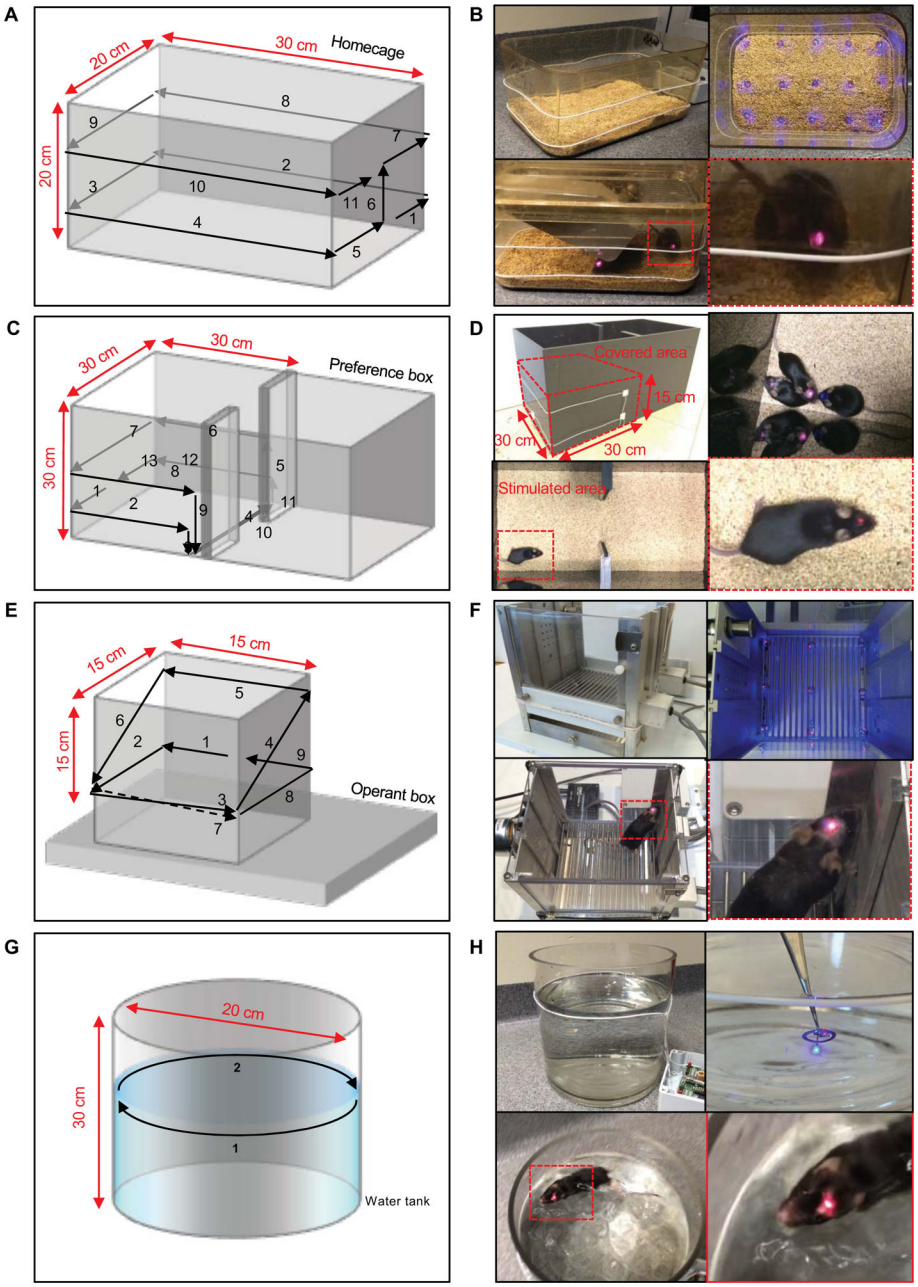

Figure 5. Representative set up of the loop antenna around various animal apparatuses

A, C, E, G) The detailed layouts of the loop around a homecage, a real-time place preference (RTPP) box, an operant conditioning box and a water tank, respectively. B) Images of the loop and wirelessly operating devices and the corresponding mice with near field wireless implants in the homecage covered with lid. D) Images of double loop and wirelessly operating devices and corresponding mice with near field wireless implants in the RTPP box. F) Images of mouse with working device in the operant conditioning chamber containing metal components. H) Images of water tank with single loop antenna, working devices under the water and a swimming mouse that has working device

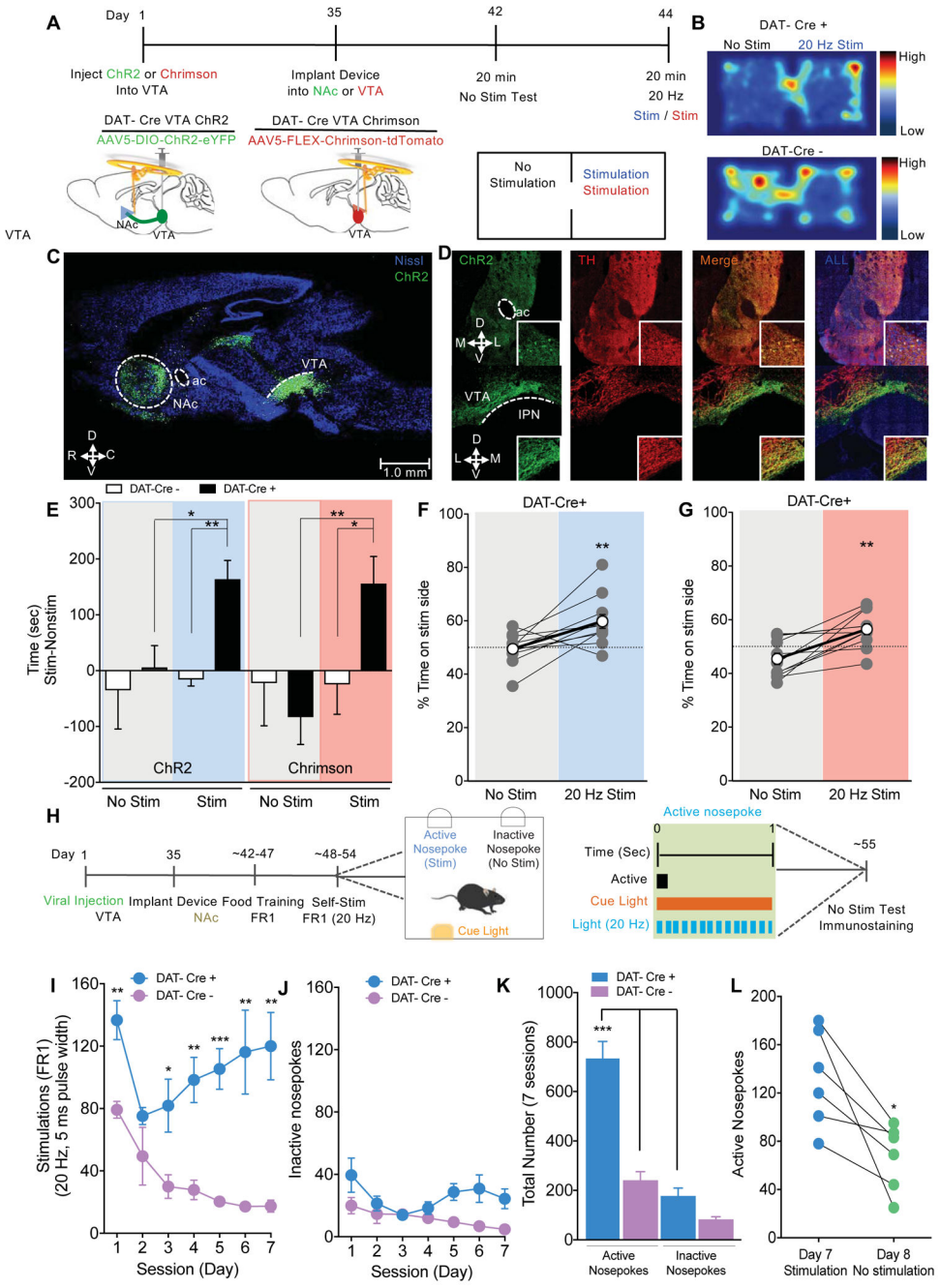

Figure 6. Wireless control of mesolimbic reward circuitry

A) Cartoon depicting unilateral ChR2 or Chrimson viral injection and near field wireless device implantation. Timeline outlining real time place preference behavioral testing. B) Heatmaps showing real-time mouse behavior following 20 Hz photostimulation of mice expressing ChR2 in the NAc of DAT-Cre+ and DAT-Cre−. C) Sagittal section highlighting ChR2 viral injection within the ventral tegmental area (VTA) and the targeted projection area of the nucleus accumbens (NAc). D) Corresponding coronal sections highlighting ChR2 viral expression within the VTA and NAc. Representative immunhistochemistry showing coronal sections of the NAc and VTA. All images show Nissl (blue), ChR2 (green), tyrosine

hydroxylase (TH, red) staining. E, F, G) Stimulation of the NAc or VTA in DAT-Cre mice expressing ChR2 or Chrimson, respectively, drives a real-time place preference in time spent in stimulation side (both stimulation side minus non-stimulation side and % time on stimulation side). Data represented as mean ± SEM, n = 12 (DAT-Cre +), n = 5 (DAT-Cre −) for ChR2; and n =11 (DAT-Cre +), n = 8 (DAT-Cre −) for Chrimson. H) Timeline outlining operant self-stimulation behavioral testing. Schematic depicting operant box paradigm where an active nosepoke results in a 1 sec, 20 Hz photostimulation accompanied by a cue light and an inactive nosepoke results in no consequence. I, J) DAT-Cre mice expressing ChR2 developed a strong preference for the active nosepoke (20 Hz photostimulation) over 7 days in comparison to the inactive nosepoke or in comparison to DAT-Cre mice lacking ChR2 expression (one way repeated measures ANOVA, main effect of nosepoke ; main effect on stimulation, Tukey post hoc tests *$p<0.05$, **$p<0.01$, ***$p<0.001$). K) Data showing total number of active and inactive nosepokes in DAT-Cre + and DAT-Cre− mice across 7 days of operant self-stimulation (Two-way ANOVA, main effect of nosepoke,; main effect on cre condition, Bonferroni post hoc tests ***$p<0.001$). L) On day 8, ChR2 expressing mice were allowed to nosepoke in the absence of photostimulation. All mice showed a reduction in number of active nosepokes in the absence of photostimulation. Data represented as mean ± SEM, n = 6 (DAT-Cre +), n = 5 (DAT-Cre).